Research Square

Preprints are preliminary reports that have not undergone peer review.
They should not be considered conclusive, used to inform clinical practice,
or referenced by the media as validated information.

Spatially Resolved Mechanical Properties of Laser Powder Bed Fused Inconel 718 by Micro-Tensile Testing: Influence of Thermal History and Microstructure

Prudhvi Raj Pola
Oklahoma State University
Kaustubh Deshmukh
Virginia Tech
Clinton Switzer
Oklahoma State University
Siddhesh Chaudhari
Oklahoma State University
Prahalada Rao
Virginia Tech
Ranji Vaidyanathan
vaidyan@okstate.edu

Oklahoma State University

Research Article

Keywords: Laser Powder Bed Fusion (L-PBF), Micro-tensile testing, Inconel 718, Local Mechanical Properties

Posted Date: November 10th, 2026

DOI: https://doi.org/10.21203/rs.3.rs-11262458/v1

License: This work is licensed under a Creative Commons Attribution 4.0 International License.
Read Full License

Additional Declarations: No competing interests reported.

Spatially Resolved Mechanical Properties of Laser Powder Bed Fused Inconel 718 by Micro-Tensile Testing: Influence of Thermal History and Microstructure

Abstract

Laser Powder Bed Fusion (L-PBF) fabricates three-dimensional parts through sequential layer deposition and melting. Each layer undergoes repeated thermal cycles, resulting in anisotropy and microstructural heterogeneity, which complicates part qualification. Characterizing this spatial variability using conventional mechanical tests requires numerous large specimens and is therefore costly and time-consuming. This study introduces a micro-scale testing framework to evaluate the local mechanical behavior of as-built L-PBF Inconel 718 parts. Miniature tensile specimens (3 mm × 1 mm × 0.25 mm) extracted from selected locations in four L-PBF geometries were used to determine local elastic modulus, yield strength, ultimate tensile strength, and strain to failure. Local mechanical properties were correlated with microstructural parameters and thermal history metrics. Significant spatial variability in mechanical properties was observed within the individual part and among the four geometries. The observed variability was more strongly correlated with thermal history metrics followed by microstructural parameters. The proposed approach enhances understanding of spatial heterogeneity in L-PBF parts and provides a basis for incorporating location-specific properties into component qualification and performance assessment.

Keywords: Laser Powder Bed Fusion (L-PBF), Micro-tensile testing, Inconel 718, Local Mechanical Properties

1 Introduction

Metal additive manufacturing (AM) has experienced significant growth in industries such as aerospace and automotive due to its capacity for efficient fabrication of geometrically complex components, which can reduce part count, assembly requirements, post-processing, and overall production costs. Adoption is further driven by the ability to tailor local microstructures by controlling processing parameters[1, 2]. n the aerospace industry, metal AM is widely utilized for its design flexibility, reduced lead times, and lightweight components, all of which support cost management. However,

certifying safety-critical parts remains challenging because current standards are not well suited to these applications and require extensive printing and testing[3]. Recent advancements in process and material systems have facilitated the integration of metal AM into commercial manufacturing [4].

Laser powder bed fusion (L-PBF) is a widely adopted metal additive process across industries because it can produce high-precision parts with good surface finish and high density. Despite these advantages, defects formed during printing have limited the broader adoption of L-PBF. Ongoing developments focus on reducing flaw formation through in-situ monitoring and process parameter adjustments [5–7].

Inconel 718 (IN 718) is a nickel-based super alloy widely used in the aerospace and oil & gas industries for its high strength and ability to maintain oxidation and corrosion resistance at temperatures approaching 700 °C. This precipitation-strengthened alloy derives much of its strength from γ' and γ'' precipitates, with additional contributions from carbides and other secondary phases. Processing conditions are critical for IN 718, as they strongly influence mechanical properties and, consequently, final component performance. Additive manufacturing enables rapid production of complex, high-precision IN 718 parts, addressing high demand and overcoming the longer lead times and geometric constraints of conventional methods [8–10].

While additive manufacturing has been adopted in various industrial applications, its use in safety-critical primary structures remains limited due to inconsistent component quality and mechanical properties [3, 11]. hese inconsistencies arise from subsurface defects, surface roughness, residual stresses, anisotropy associated with layer-wise deposition, and repeated thermal cycles during solidification, all of which affect microstructure and mechanical performance [12]. Anisotropy and heterogeneity in metal AM are influenced by process parameters such as beam size, beam power, scan speed, and processing temperature, as well as deposition rate, scan strategy, material type, and particle size distribution. Anisotropy primarily results from the complex microstructure formed during fabrication, which produces epitaxial columnar grains oriented parallel to the build direction and heterogeneity driven by thermal gradients. [13–17].

Understanding the process-structure-property relationship is essential, as the performance of metal AM parts depends on their microstructure and resulting mechanical properties [11]. Knowledge of the as-fabricated microstructure and its influence on part properties remains important even after post-processing. Improved understanding of the as-fabricated microstructure enables more effective process adjustments [18].

A workshop convened by the National Academies of Sciences, Engineering, and Medicine highlighted that the properties and microstructure of AM components are highly sensitive to process parameters and part geometry, resulting in significant local variations. Testing large coupons does not accurately represent the properties of the entire part or capture local effects. Douglas Hofmann of the National Aeronautics and Space Administration (NASA's) Jet Propulsion Laboratory noted that qualifying a specific alloy for space applications can cost over $2 million [19].

In current industrial practice, mechanical characterization of metal additive-manufactured parts relies mainly on bulk specimens, which provide only average properties. However, witness coupons, including specimens tested according to ASTM

E8/E8M, may not accurately represent the properties of the corresponding printed component. Significant anisotropy and property variation arise from differences in thermal history and a heterogeneous microstructure, both inherent to the additive manufacturing process. As William E. Frazier noted, certifying parts produced through this process can cost millions of dollars for a given application[20, 21].

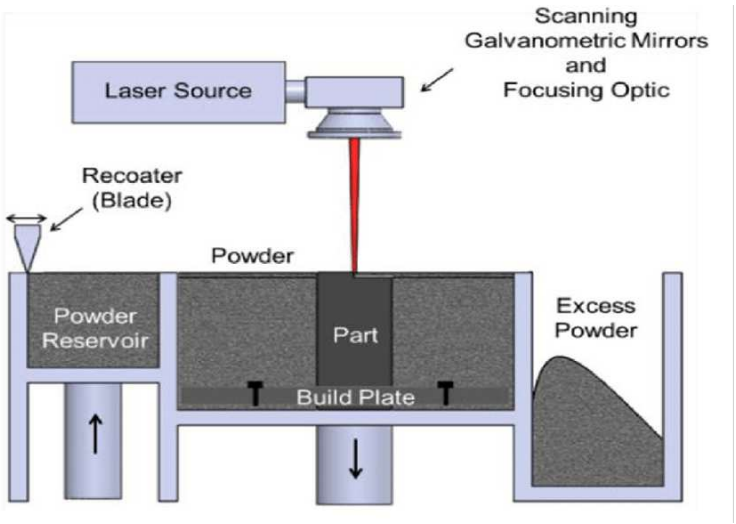


Fig. 1 Schematic of Laser Powder Bed Fusion (L-PBF) Process [22]

Previous studies have reported substantial property variation among nominally identical parts produced within the same build, as well as differences between additively manufactured and wrought material. As shown in Table 1, most studies of additively manufactured (AM) parts employs traditional methods, which provide only average mechanical properties of test coupons and do not accurately reflect the behavior of large-scale components. Mechanical properties are typically evaluated based on processing conditions, orientation effects, porosity, and microstructure. Existing research primarily relies on macro-scale coupon testing and correlates the resulting properties with processing parameters, build orientation, porosity, and microstructure.

This study evaluates location-specific mechanical properties in four L-PBF IN718 geometries using micro-tensile specimens measuring 3 mm × 1 mm × 0.25 mm. The measured properties are correlated with location-specific thermal-history metrics (end-of-cycle temperature and cooling time), and microstructural characteristics, including grain size, aspect ratio, and crystallographic texture.

2 Materials and Methods

2.1 Printing Setup

Laser powder bed fusion (L-PBF) is a layer-by-layer process in which a layer of powder of a defined thickness is spread over the substrate or previously consolidated layers,

Table 1 Summary of previous studies examining mechanical properties, specimen dimensions, and correlations with microstructure.

Reference	Mechanical Testing	Sample Dimensions	Study objective
Kim, Allen, et al. [2]	Nano-Hardness	-	Nano-Hardness was measured and correlated with microstructure in the as-built and heat-treated conditions.
Deng, Dunyong, et al [10]	Vickers microhardness and Tensile Testing	30mm x 8mm x 2 mm	Studied the effect of sample orientation on the mechanical properties, primarily tensile strength and elongation.
Varney, Tracy Connor, et al. [23]	Tensile testing	10mm x 6mm x 0.8(0.6)mm	Compared as-printed thin-wall specimens with specimens extracted from bulk material and correlated the results with microstructure and scan strategy.
Wang, Xiaoqing, and Kevin Chou [24]	-	-	A staircase Inconel 718 block was fabricated to investigate the effects of the thermal cycles on the microstructure evolution in the Selective laser melting (SLM).
Popovich, V. A., et al. [25]	Vickers Hardness and Tensile testing	50 mm long tensile bar	Application of suitable process parameters and laser sources in SLM may favor either one sharp single component texture, more uniformly distributed crystal orientation, or a combination of the above in a preferred gradient, which influences the mechanical properties.
Zhang, Dongyun, et al. [26]	Tensile Testing	75 mm long and 5 mm in diameter	Samples produced by SLM were heat-treated using industrial standard heat treatments for IN718 castings and forgings to evaluate changes in microstructure, phase precipitate, and mechanical properties.
Liu, Fencheng. et al. [27]	Tensile testing and Vickers micro-hardness	20 mm gage section and 3 mm diameter	Effect of Laser scan path on mechanical properties and correlation with microstructure.
Zhao,Xiaoming, et al. [28]	Tensile testing	71 mm long, 5 mm in diameter	Investigation on the microstructure and mechanical properties of laser rapid forming IN718 deposited.
Trosch, Tanja, et al. [9]	Tensile Testing	8 mm long and 1 mm thick	Mechanical properties of as-printed and heat-treated SLM parts compared with forged and as-cast parts.

and then melted by a laser, as shown in Figure 1. Four geometries—NIST Overhang, VT, Cone, and Cuboid were fabricated using an SLM H280 Laser Powder Bed Fusion machine, as shown in Figure 2. This cycle continues until each part was completed in

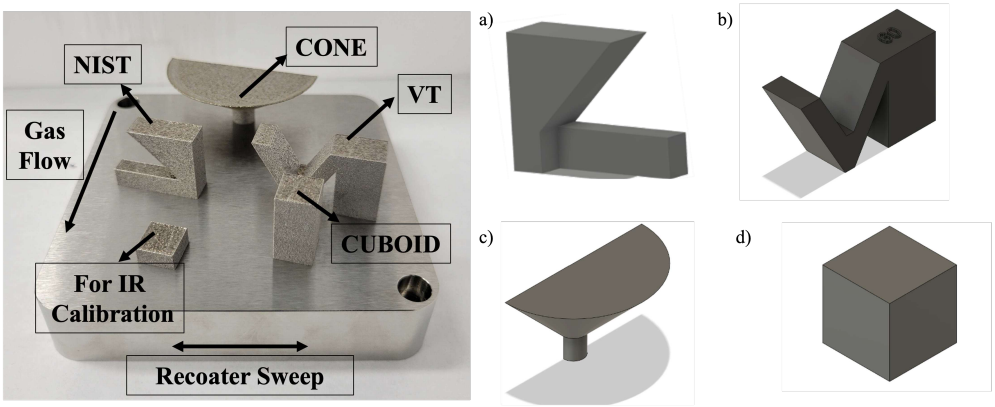


Fig. 2 As-built parts on the stainless steel build plate: a) NIST Overhang, b) VT, c) Cone, and d) Cuboid

accordance with the digital model. The feedstock material was Inconel 718 from Praxair Technologies, with a powder size range of 15 to 45 μm. All parts were fabricated on a stainless-steel build plate to a maximum height of 20 mm. These geometries were selected to study how geometry influences quality metrics. The processing parameters are listed in Table 2.

Table 2 Process Parameters

Parameter	Value
Laser Power	200 W
Scan Speed	1000 mm/s
Layer Height	0.03 mm
Hatch Spacing	0.09 mm
Layer Rotation	67°
Scan Pattern	Bi-directional stripes

2.2 Thermal modeling

Process parameters, part geometry, scan strategy, and additional factors significantly influence heat accumulation and dissipation during metal additive manufacturing. These variables govern the part's thermal history, including local temperature distributions and cooling rates, which subsequently influence microstructure development at each location. Predicting temperature distributions requires solving the heat diffusion equation. Although a finite element-based approach is commonly employed for this purpose, it is both time-consuming and computationally expensive [29–34].

A meshless analysis based on graph theory was used to calculate the temperature distribution in the part. The geometry is divided into nodes, which are connected to

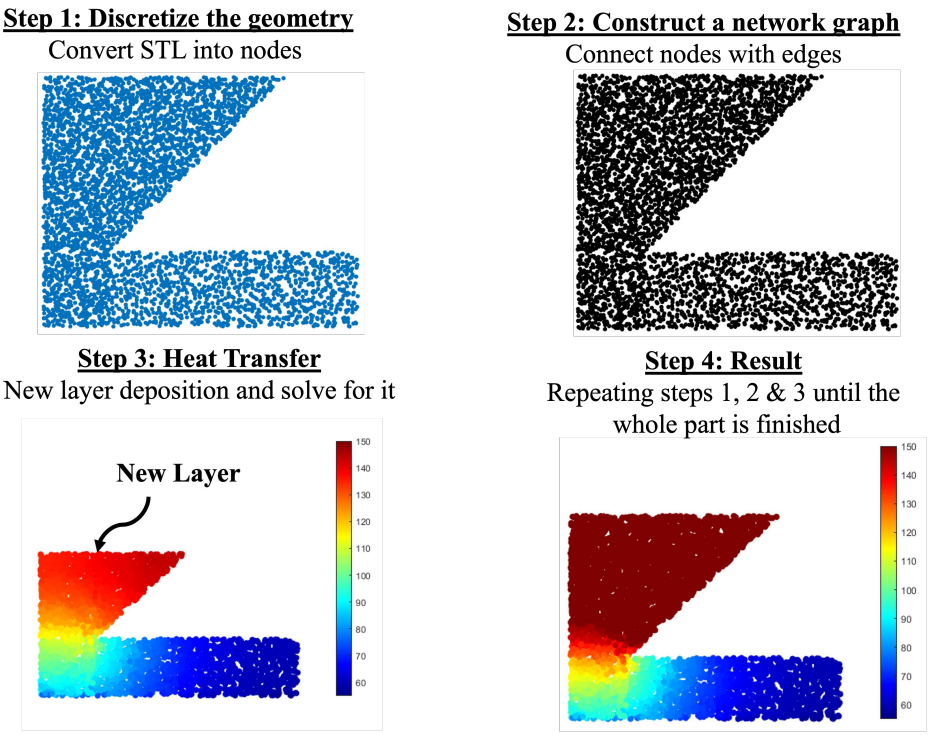


Fig. 3 Schematic of the meshless graph-theory method used to calculate part-scale thermal-history metrics

form a network graph. Each newly deposited layer was simulated, and the corresponding temperature field and cooling behavior were calculated. This process is repeated for every layer until the part is finished, as shown in Figure 3. The model provides the End of Cycle (EOC) Temperature (T_e), defined as the average surface temperature of a layer after a new layer of powder is added. Cooling time (t_c) was defined as the time required for a location to cool from 1600 °C to 700 °C, as illustrated in Figure 4. The method predicts part-scale temperature distributions and cooling behavior in less than 5 min, with a reported error of less than 5% relative to experimental measurements error [29, 31–35].

2.3 Micro-sample extraction

Micro-tensile specimens measuring 3 mm x 1 mm x 0.25 mm, as shown in Figure 5, were extracted from four geometries using Micro Wire-Electrical discharge machining (Wire-EDM) process (Figure 6). Since each sample went through a three-pass Wire-EDM process, surface roughness was considered to have minimal effect on the measured properties.

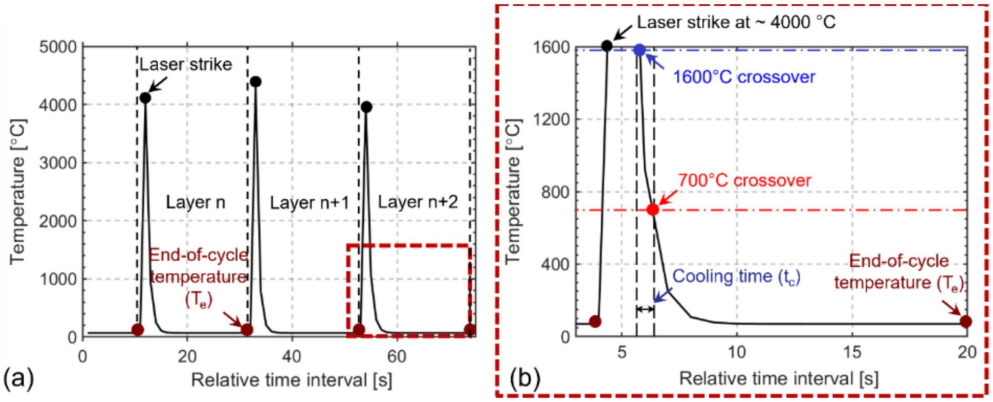


Fig. 4 Schematic showing the representative thermal cycling (a) over three-layer scans as a result of the laser strike and a subsequent cool-down period, (b) over an individual laser scan in the L-PBF process, this work estimates the cooling time (t_c) for a layer to cool down from 1600 °C to 700 °C and the end of cycle temperature (T_e)[22].

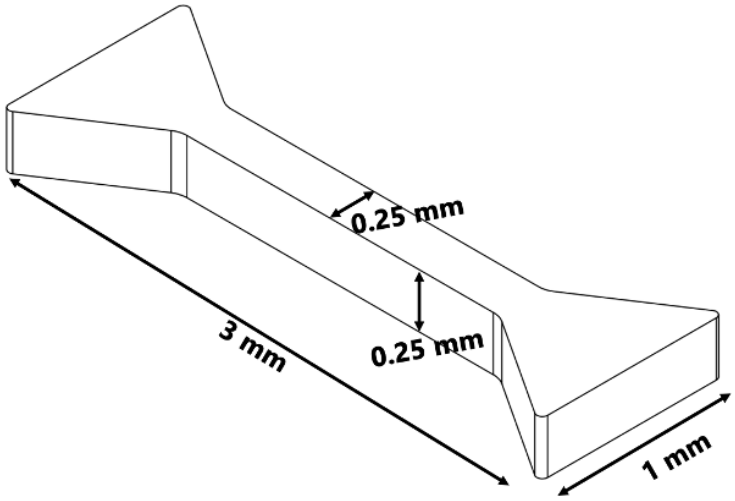


Fig. 5 Schematic of Micro-sample with dimensions

2.4 Metallography

Following the extraction of micro-samples, additional material sections were extracted from the same build layer adjacent to each micro-tensile specimen, to perform microstructural characterization at that location. Each sample was mounted in a mixture of quickset acrylic powder, liquid, and graphite powder to ensure conductivity during microscopy. This cold mounting process required approximately 10 minutes per sample. After mounting, up to six samples were polished simultaneously using a

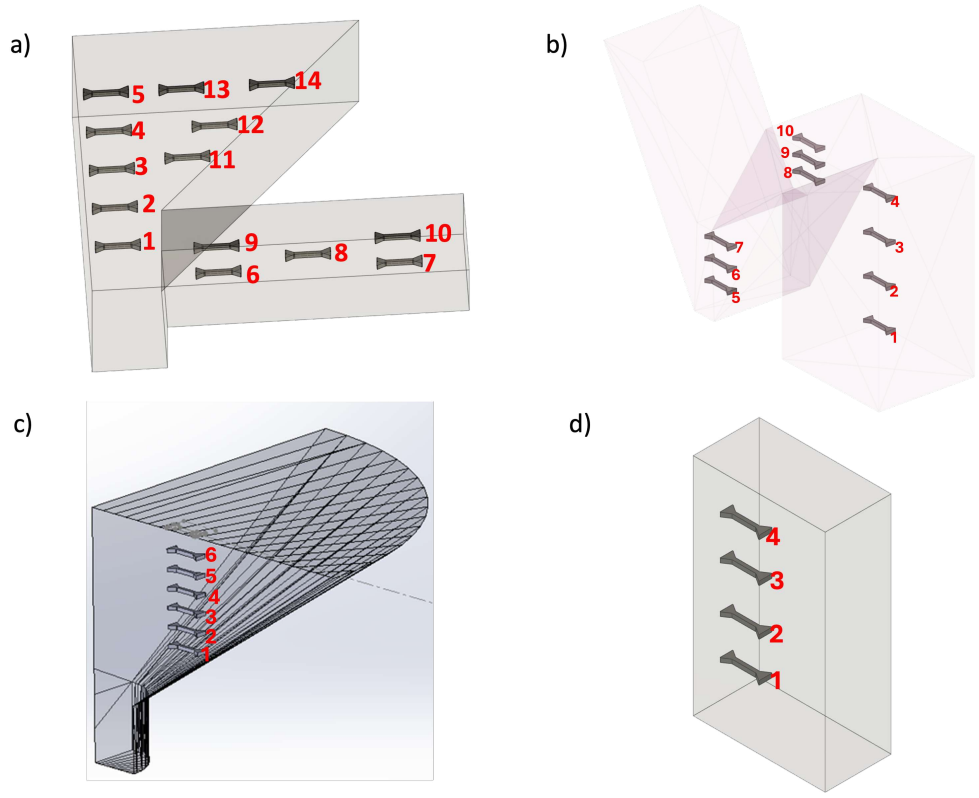


Fig. 6 Locations and Orientations of micro-tensile specimens extracted from the a) NIST overhang, b) VT, c) Cone, and d) Cuboid

Buehler Automet 250 semi-automatic polisher. Due to the thinness of the samples, initial polishing was performed with 400-grit paper for 30 seconds, followed by 600, 800, and 1200 grit papers for one minute each to clean the surfaces. Subsequent polishing steps included applying 9 µm and 3 µm diamond polishing suspensions for 10 minutes each to remove surface scratches. The pre-final polishing stage used 1 µm and 0.3 µm alumina suspensions. Finally, a 0.05 µm colloidal silica suspension was applied until a mirror-like surface finish was achieved, suitable for Electron back scattered diffraction (EBSD) analysis.

2.5 Microstructural characterization

Electron Backscattered Diffraction (EBSD) was used to determine grain size, aspect ratio, and preferred crystallographic texture at each location. A Scios2 LoVac field-emission gun scanning electron microscope (SEM) equipped with Quasor II EBSD (ThermoFisher Scientific, Hillsboro, Oregon, USA) was used. The mounted specimen was tilted by 70 degrees for EBSD characterization, as shown in Figure 7. To ensure conductivity, one edge of the sample was attached to carbon tape and grounded to the

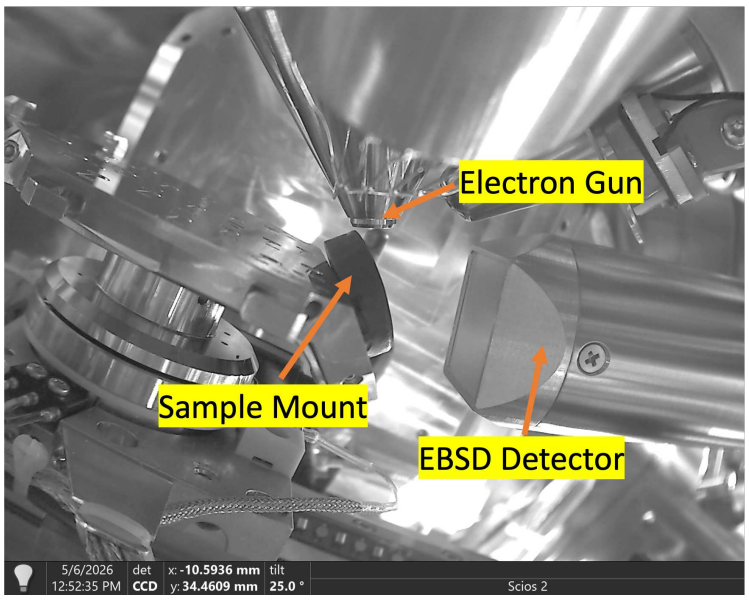


Fig. 7 Sample mounted on the stage in Scanning Electron Microscope(SEM) for Electron Backscattered Diffraction (EBSD) analysis

bottom of the sample. Images were captured with a 45 ms exposure time and a step size of 0.49 μm. The scan area was kept constant at 254 x 196 mm^2 for all samples, matching the micro-sample cross-section. The EBSD data were post-processed using Pathfinder (version 2.10) software.

2.6 Micro-tensile testing

Each specimen was tested using an in-house micro-tensile system, as shown in Figure 8. Originally designed for micro-electromechanical systems (MEMS) and welding applications, the setup was later adapted to evaluate the local mechanical properties of metal additively manufactured components[36–41]. It includes an actuator, load cell, linear air bearing, precision micro-sample grips, and a high-resolution imaging system. Digital image correlation (DIC) was used to measure axial strain and full-field deformation during testing. Tests were conducted at a nominal strain rate of 10^{-3}/s with a gauge length of 1.58 mm for each specimen. Vic-Snap and VIC 2D-7 software from Correlated Solutions were used for testing and post-processing to calculate strain. VIC 2D-7 settings are provided in Table 3. With respect to the specimen size effect, the specimen utilized in the present study to characterize spatial properties is appropriately qualified and accurately reflects the bulk properties as reported in the literature [42].

A fine speckle pattern was applied using an airbrush. The specimen surface was first coated with a thin white background layer, after which black speckles were applied. Speckle size and spatial distribution were controlled by adjusting the air pressure and the distance between the airbrush and the specimen.

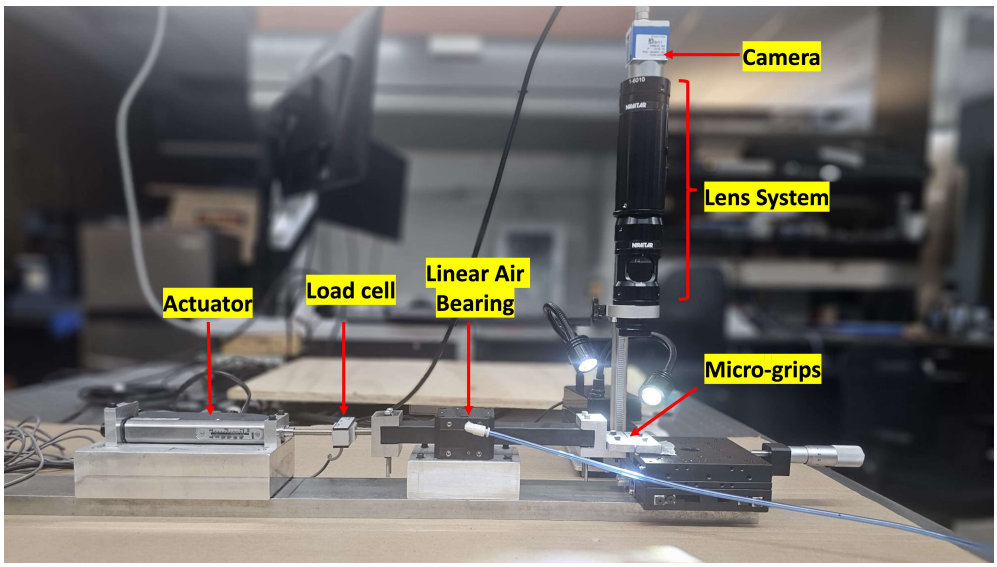


Fig. 8 Micro-Sample Experimental Setup with Digital Image Correlation(DIC)

Table 3 DIC Analysis settings

Parameter	Value
Subset size	35-55
Step size	7
Interpolation	Optimized 8-tap
Correlation Criterion	Normalized square differences
Subset weights	Gaussian
Exhaustive search	Disabled
Low-pass filter images	Disabled
Incremental Correlation	Enabled
Prediction margin (pixel)	0.02
Confidence interval (pixel)	0.1
Matchability (pixel)	0.1
Filter	Decay filter
Filter size	15

3 Results

3.1 Mechanical Properties

Figure 9 shows the stress-strain behavior of micro-samples extracted from four geometries. The results demonstrate distinct levels of spatial variability among the geometries. NIST exhibits significant variability, with locations displaying both the highest and lowest values for strength and elongation. In contrast, the cone shows relatively consistent values across sampling locations, with only minor differences in failure

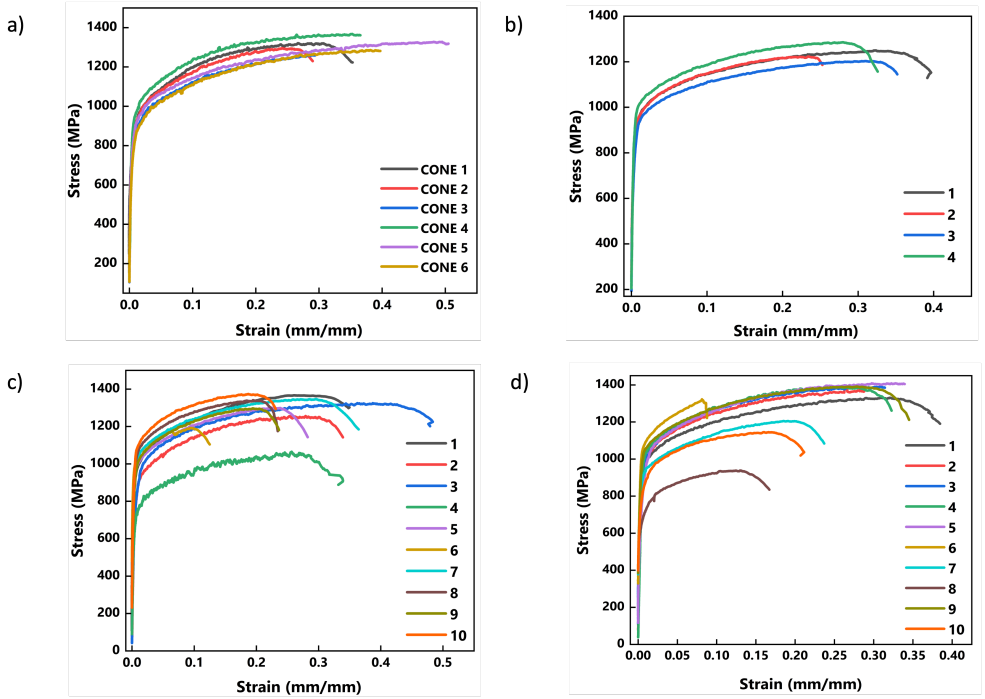


Fig. 9 Stress-Strain behavior: a) CONE, b) Cuboid, c) VT, and d) NIST

strain. VT displays pronounced variation in both strength and ductility throughout the part. The cuboid is considerably more consistent, exhibiting relatively small differences. These findings indicate that mechanical properties vary spatially within each geometry and are dependent on the specific geometry examined.

Ideally, stress-strain curves should overlap, as they originate from the same material and part. However, the curves do not overlap in every instance and differ from location to location, a process inherent to additive manufacturing. These variations arise because layers are repeatedly heated and cooled during printing, altering the microstructure until the part is complete. Heat retention in the part after printing also contributes significantly to spatial variation. Additionally, ductility varies because small voids form during the process.

Figure 10(a) presents the elastic modulus values for specimens with NIST, Cone, VT, and Cuboid geometries. The box plots illustrate the mean, median, inter-quartile range, overall spread, and individual measurements for each geometry. Cuboid specimens exhibited the highest median elastic modulus, approximately 225 GPa, and the smallest inter-quartile range, indicating high repeatability and minimal variation. VT specimens also demonstrated high elastic modulus values but displayed a much higher spread. The presence of an outlier above 320 GPa suggests that local microstructural differences may have affected the measured stiffness. NIST specimens showed

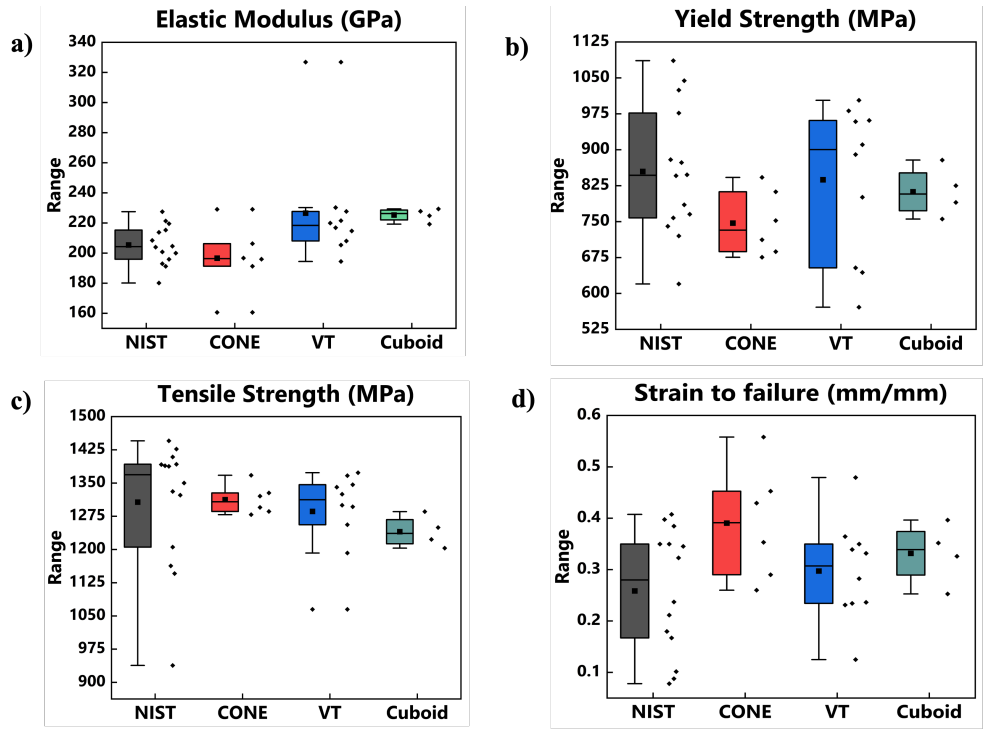


Fig. 10 Variability of Mechanical Properties within and across the geometries (NIST, CONE, VT, Cuboid)

a moderate modulus with some variability, whereas Cone specimens had the lowest median elastic modulus. Despite the lower average stiffness of Cone specimens, their measurements were consistent, as indicated by the narrow distribution. These findings indicate that specimen geometry significantly affects the measured elastic modulus. Cuboid geometry yields the most repeatable stiffness measurements, while VT geometry appears more sensitive to local material differences.

Yield strength distributions for the four geometries are shown in Figure 10(b). Yield strength is the stress at which permanent plastic deformation begins, and it is important for understanding how much load a material can handle. VT specimens had the highest median yield strength, close to 900 MPa, but their results varied the most, ranging from about 560 MPa to nearly 1000 MPa. This wide range suggests that differences in microstructure and residual stresses play a significant role in when yielding starts. NIST specimens also showed high yield strength with a lot of variation, which points to inconsistent local mechanical behavior. On the other hand, Cone specimens had the lowest median yield strength, around 730 MPa, and their results were more tightly grouped. Cuboid specimens fell in the middle for yield strength and showed fairly consistent results, which suggests a good balance between strength and repeatability. Overall, these findings show that specimen shape affects both strength and the extent of variability in results.

Figure 10(c) shows the ultimate tensile strength (UTS) results for each specimen shape. Ultimate tensile strength is the maximum stress a material can handle before it starts to thin and break. The NIST specimens had the highest average tensile strength, about 1360 MPa, but also showed a lot of variation, with some specimens having much lower strengths. The VT specimens exhibited relatively high tensile strength, with moderate variation and an outlier. The Cone specimens had a slightly lower average tensile strength but the least variation, indicating highly consistent results. The Cuboid specimens had the lowest average tensile strength among the four shapes but showed a fairly tight range, indicating steady performance. This variability may be due to small defects, pores, or structural irregularities. While the NIST shape achieves the highest tensile strength, the Cone and Cuboid shapes provide more consistent results.

Figure 10(d) shows a comparison of how much the four specimen shapes stretch before breaking. The Cone specimens had the highest average stretch before breaking, about 0.39 mm/mm, and the widest range of values, showing they are more flexible than the other shapes. Cuboid specimens also had fairly high stretch values with a smaller range, showing steady, consistent behavior. VT specimens had medium elongation with some variation. In contrast, NIST specimens had the lowest average stretch before breaking and the widest overall range. The wide range of NIST specimens shows a lot of differences between samples, possibly due to small structural differences. These results show that specimen shape affects both the measured strength and how flexible the material seems.

The observed differences across locations among the four geometries arise from the shapes of each geometry, which influence thermal gradients. These thermal gradients subsequently alter the microstructure at each location. As a result, these parameters affect the part's mechanical properties and performance at each location.

3.2 Microstructural analysis: Crystallographic texture, grain size and aspect ratio

At each micro-sample location, grain size and aspect ratio were quantified using EBSD. This technique also provides crystallographic texture and grain structure at the same location, enabling the identification of changes in preferred orientation across different positions within the geometry.

Grain size was calculated using a minimum misorientation angle of 10 degrees and a minimum grain area of 5 pixels at all locations. The aspect ratio ranges from 0 to 1, where an aspect ratio of 1 represents an equiaxed grain, whereas values approaching 0 represent increasingly elongated grains. Most locations exhibit aspect ratios between 0.4 and 0.5, indicating moderately elongated grains. In the Cone geometry, three locations exhibit aspect ratios below 0.4, indicating highly elongated grains, likely resulting from thermal gradients induced by the geometry. The lower locations in the NIST geometry, positions 6–10, exhibited aspect ratios greater than 0.5, which may be associated with increased heat extraction and more rapid cooling.

At NIST 2 location, grains are large and slightly elongated. At NIST 4, the grains show columnar morphology and also exhibits epitaxial grain growth, which is inherent to the layer-by-layer process. NIST 8, closest to the substrate, displays a finer grain

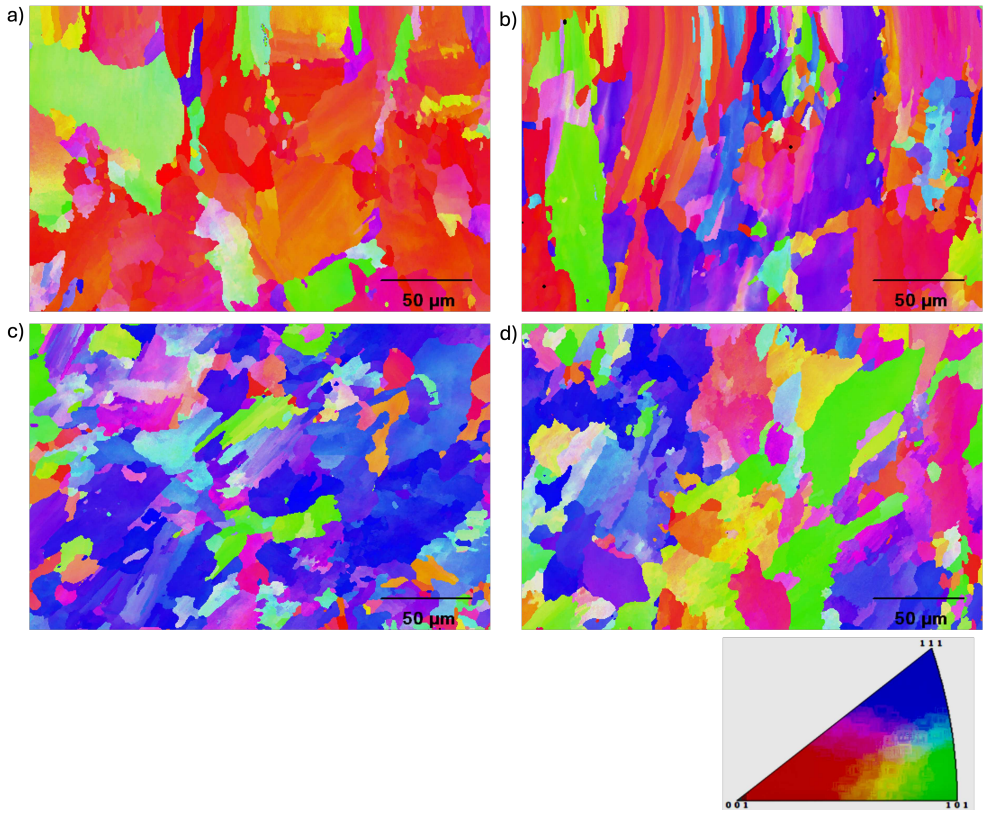


Fig. 11 EBSD maps representing grain structure at a) NIST 2, b) NIST 4, c) NIST 8, d) NIST 13

structure because cooling rates are faster with the substrate acting as a heat sink. NIST 13, at the overhang, shows a combination of columnar and equiaxed structures with slanted grains due to heat distribution in that region as shown in Figure 11. Overall, grain morphology changes from finer to coarser and some locations show columnar grain morphology. These changes indicate that local geometric features, such as base versus overhang, influence solidification criteria and alter the microstructure. This leads to anisotropic behavior across the part. These differences across locations arise from heat retention in the part, as lower sections retain less heat than higher ones, and this changes with geometry.

Preferred crystallographic orientation was examined at each location to assess spatial variation. Figure 12 presents the preferred crystallographic orientations at three locations within the NIST geometry. In the normal direction, a clear change in preferred orientation is observed: at NIST 2, $< 001 >$ is dominant; at NIST 8, $< 111 >$ is preferred; and at NIST 13, $< 101 >$ is the primary orientation. In the specimen loading direction, a transition from $< 001 >$ to $< 101 >$ is evident, with some locations exhibiting mixed orientations. The transverse direction also shows clear changes in the preferred grain orientation across different locations. Variations in preferred

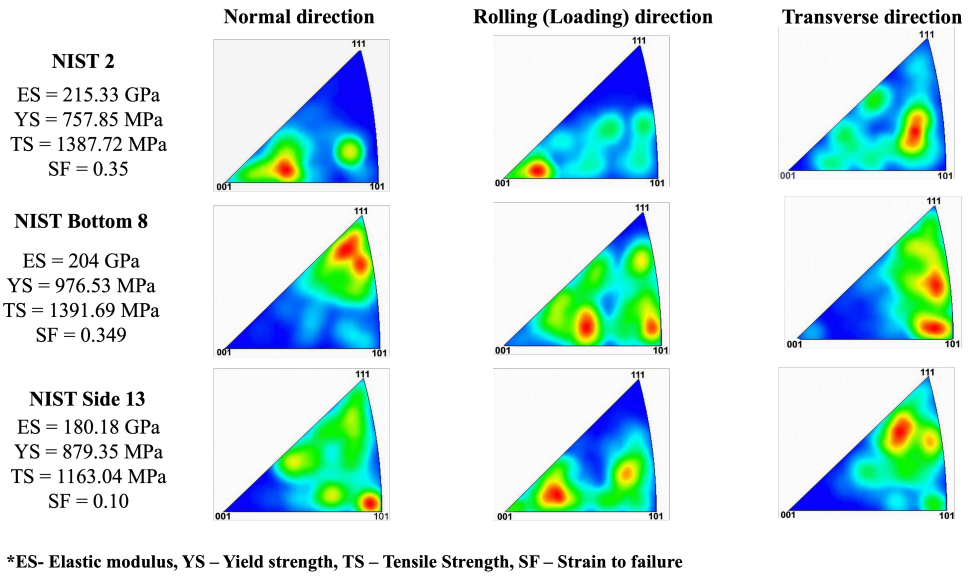


Fig. 12 Preferred Crystallographic Orientations in NIST at three locations (NIST 2, NIST 8, NIST 13)

orientation across locations significantly influence the mechanical properties at each site. Changes in modulus are directly correlated with shifts in preferred orientation, as illustrated in Figure 12. Specifically, in the normal direction, $< 001 >$ orientations exhibit higher moduli, whereas $< 101 >$ orientations correspond to lower moduli. Similar trends are observed for other mechanical properties, including yield strength and tensile strength.

4 Relationships among thermal history, microstructure, and mechanical properties

4.1 Thermal History vs Microstructure

The Pearson correlation matrix (Figure 13) demonstrates that the thermal history variables, end-of-cycle temperature (EOC) and cooling time, exhibit the strongest relationship, with a positive correlation coefficient of 0.70. This strong correlation suggests that locations with higher end-of-cycle temperatures generally require longer cooling times, reflecting the inherent thermal behavior characteristic of the LPBF process. Both thermal parameters exhibit moderate to strong correlations with the measured microstructural features. EOC displays a moderate negative correlation with grain size (r = -0.54) and a strong negative correlation with aspect ratio (r = -0.69), indicating that increased thermal accumulation is associated with finer and less elongated grains. Similarly, cooling time is negatively correlated with grain size (r = -0.44) and aspect

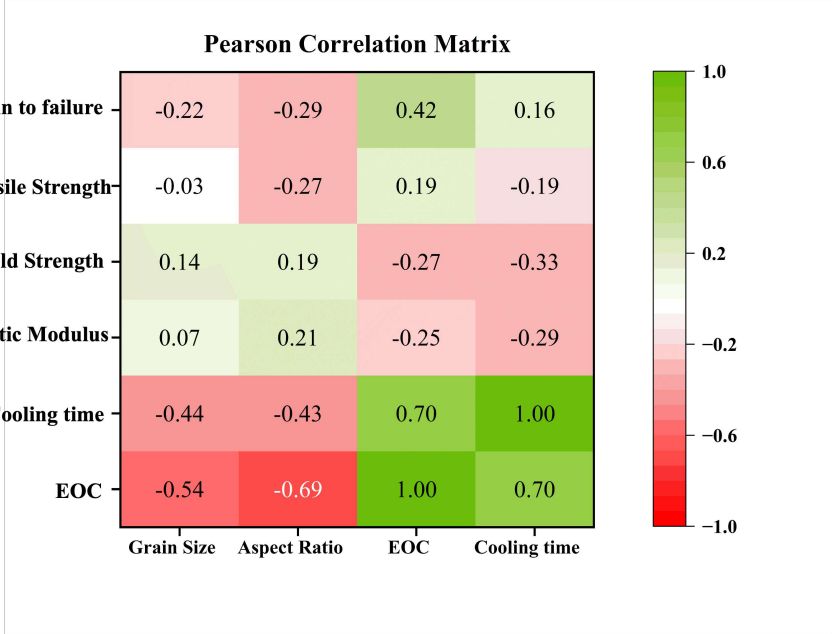


Fig. 13 Correlation between the Thermal gradients, Microstructural parameters, and Mechanical Properties

ratio (r = -0.43), suggesting that thermal history significantly influences the resulting microstructure.

Principal component analysis (PCA) was conducted to examine the correlation between thermal gradients and microstructural parameters, specifically grain size and aspect ratio, as shown in Figure 14. The results indicate that thermal history differentiates the geometrical aspects, with the cone geometry exhibiting higher EOC temperatures and longer cooling times because of geometry-dependent heat accumulation. Thermal history metrics, including end-of-cycle (EOC) temperature and cooling time, serve as primary drivers of changes in microstructural parameters such as grain size and aspect ratio. These microstructural parameters exhibit an inverse relationship with thermal gradients, suggesting that increases in EOC and cooling time are associated with reductions in grain size and aspect ratio. The NIST geometry demonstrates the greatest variation in grain size and aspect ratio, followed by VT.

4.2 Thermal History & Microstructure vs Mechanical Properties

Principal component analysis (PCA)(Figure 15) and Pearson correlation (Figure 13) analyses were performed to examine relationships among thermal-history metrics, microstructural characteristics, and mechanical properties. Mechanical properties show weak links with thermal and microstructure-related factors, indicating that several interacting elements affect local mechanical behavior. Strain to failure shows the strongest positive link with EOC (r = 0.42) and a weaker positive link with cooling

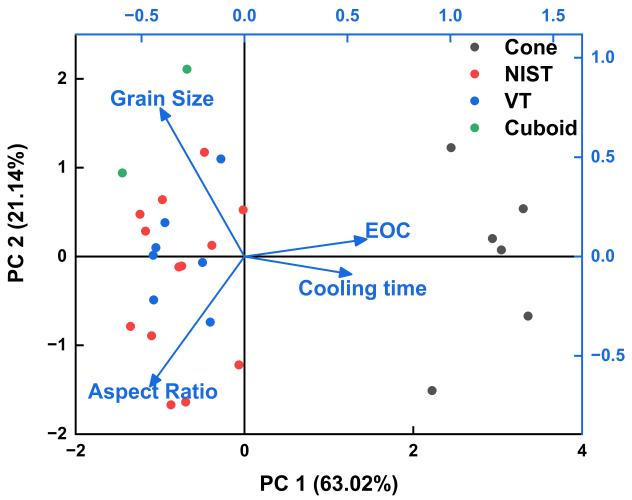


Fig. 14 Principal Component Analysis of Thermal gradients and Microstructure

time (r = 0.16). These results suggest that areas with greater heat buildup usually have better ductility. On the other hand, yield strength and elastic modulus show weak positive links with grain size and aspect ratio (maximum r = 0.21), and weak negative links with EOC and cooling time (from -0.19 to -0.33). Tensile strength follows a similar pattern, showing only weak links to all variables studied.

The results from PCA also indicate that yield strength is inversely related to thermal gradients, particularly cooling time, and directly related to grain size. Conventionally, higher cooling rates are associated with finer microstructures; however, this relationship does not hold in the present study. The Hall-Petch relationship posits that grain size is inversely related to yield strength, implying that yield strength should increase as grain size decreases. In contrast, the present dataset shows a weak positive correlation between grain size and yield strength. This outcome suggests that, since IN 718 is a precipitation-strengthened alloy, additional strengthening mechanisms may influence yield strength. Tensile strength exhibits a slight positive relationship with thermal gradients and shows no correlation with microstructural parameters. In most cases, tensile strength appears independent of these variables. Yield strength and elastic modulus showed weak positive correlations with grain size and aspect ratio and weak negative correlations with EOC temperature and cooling time. Strain to failure showed a moderate positive correlation with EOC temperature and weaker relationships with the remaining variables. Among all geometries examined, the NIST Overhang exhibits the greatest internal variation across different locations, followed by VT, Cone, and Cuboid.

Pearson correlation and principal component analysis (PCA) consistently indicate that temperature patterns are the main factor controlling how the material's structure changes in the L-PBF processing. Higher temperatures at the end of the cycle and longer cooling times are linked to regular changes in grain size and shape. While these

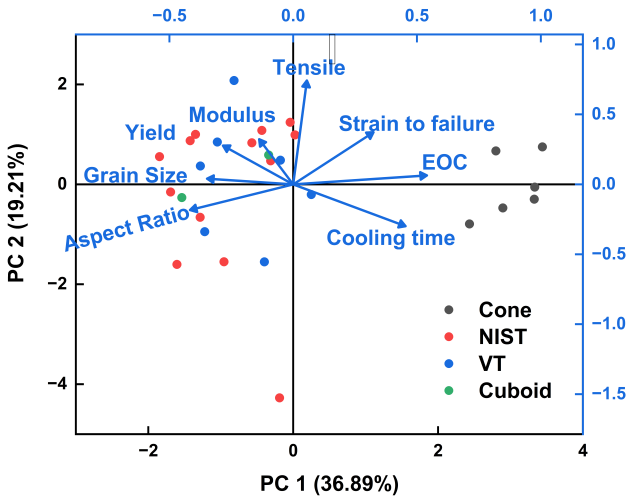


Fig. 15 Principal Component Analysis of Thermal gradients, Microstructural parameters, and Local Mechanical properties

temperature effects affect local mechanical properties, the fairly weak connections suggest that local mechanical behavior comes from a mix of temperature history, changes in structure, and other local factors like crystallographic texture and residual stress.

5 Conclusions

1. Within a single part, local mechanical properties varied substantially among individual components and were linked to differences in thermal history and microstructure. The stress-strain behavior clearly shows spatial variation both within and between parts.

2. Among the variables examined, thermal-history metrics showed the strongest associations with local mechanical properties, while grain size and aspect ratio showed comparatively weaker relationships.

3. Thermal history primarily determines the properties, particularly end-of-cycle temperature and cooling time, which affect solidification and subsequent thermal cycling. Microstructural parameters, including preferred crystallographic orientations, grain size, and aspect ratio, also affect the final mechanical properties.

4. The location-specific testing framework identifies relatively weak regions in additively manufactured (AM) components, highlighting areas more susceptible to these local variations than conventional bulk witness coupons alone.

Future research will examine the effect of processing conditions for a single geometry and investigate how processing conditions, thermal history, and microstructure influence local mechanical properties.

References

[1] Yan, F., Xiong, W., Faierson, E.J.: Grain structure control of additively manufactured metallic materials. Materials **10**(11), 1260 (2017). https://doi.org/10.3390/ma10111260

[2] Kim, A., Vu, L., Chung, T., Song, D., Wang, J.: Correlation of microstructure and nanomechanical properties of additively manufactured inconel 718. Journal of Applied Mechanics **90**(12), 121006 (2023). https://doi.org/10.1115/1.4062776

[3] Blakey-Milner, B., Gradl, P., Snedden, G., Brooks, M., Pitot, J., Lopez, E., Leary, M., Berto, F., Du Plessis, A.: Metal additive manufacturing in aerospace: A review. Materials & Design **209**, 110008 (2021). https://doi.org/10.1016/j.matdes.2021.110008

[4] Frazier, W.E.: Metal additive manufacturing: a review. Journal of Materials Engineering and performance **23**(6), 1917–1928 (2014). https://doi.org/10.1007/s11665-014-0958-z

[5] DebRoy, T., Wei, H.L., Zuback, J.S., Mukherjee, T., Elmer, J.W., Milewski, J.O., Beese, A.M., Wilson-Heid, A., De, A., Zhang, W.: Additive manufacturing of metallic components–process, structure and properties. Progress in materials science **92**, 112–224 (2018). https://doi.org/10.1016/j.pmatsci.2017.10.001

[6] Mostafaei, A., Zhao, C., He, Y., Ghiaasiaan, S.R., Shi, B., Shao, S., Shamsaei, N., Wu, Z., Kouraytem, N., Sun, T., *et al.*: Defects and anomalies in powder bed fusion metal additive manufacturing. Current Opinion in Solid State and Materials Science **26**(2), 100974 (2022). https://doi.org/10.1016/j.cossms.2021.100974

[7] Snow, Z., Nassar, A.R., Reutzel, E.W.: Invited review article: Review of the formation and impact of flaws in powder bed fusion additive manufacturing. Additive Manufacturing **36**, 101457 (2020). https://doi.org/10.1016/j.addma.2020.101457

[8] Hosseini, E., Popovich, V.A.: A review of mechanical properties of additively manufactured inconel 718. Additive Manufacturing **30**, 100877 (2019). https://doi.org/10.1016/j.addma.2019.100877

[9] Trosch, T., Strößner, J., Völkl, R., Glatzel, U.: Microstructure and mechanical properties of selective laser melted inconel 718 compared to forging and casting. Materials letters **164**, 428–431 (2016). https://doi.org/10.1016/j.matlet.2015.10.136

[10] Deng, D., Peng, R.L., Brodin, H., Moverare, J.: Microstructure and mechanical properties of inconel 718 produced by selective laser melting: Sample orientation dependence and effects of post heat treatments. Materials Science and Engineering: A **713**, 294–306 (2018). https://doi.org/10.1016/j.msea.2017.12.043

[11] Zuback, J., Debroy, T.: The hardness of additively manufactured alloys. Materials **11**(11), 2070 (2018). https://doi.org/10.3390/ma11112070

[12] Seifi, M., Salem, A., Beuth, J., Harrysson, O., Lewandowski, J.J.: Overview of materials qualification needs for metal additive manufacturing. Jom **68**(3), 747–764 (2016). https://doi.org/10.1007/s11837-015-1810-0

[13] Lewandowski, J.J., Seifi, M.: Metal additive manufacturing: a review of mechanical properties. Annual review of materials research **46**(1), 151–186 (2016). https://doi.org/10.1146/annurev-matsci-070115-032024

[14] Kok, Y., Tan, X.P., Wang, P., Nai, M.L.S., Loh, N.H., Liu, E., Tor, S.B.: Anisotropy and heterogeneity of microstructure and mechanical properties in metal additive manufacturing: A critical review. Materials & Design **139**, 565–586 (2018). https://doi.org/10.1016/j.matdes.2017.11.021

[15] Carroll, B.E., Palmer, T.A., Beese, A.M.: Anisotropic tensile behavior of ti–6al–4v components fabricated with directed energy deposition additive manufacturing. Acta Materialia **87**, 309–320 (2015). https://doi.org/10.1016/j.actamat.2014.12.054

[16] Gockel, J., Beuth, J., Taminger, K.: Integrated control of solidification microstructure and melt pool dimensions in electron beam wire feed additive manufacturing of ti-6al-4v. Additive Manufacturing **1**, 119–126 (2014). https://doi.org/10.1016/j.addma.2014.09.004

[17] Kelly, S., Kampe, S.: Microstructural evolution in laser-deposited multilayer ti-6al-4v builds: Part ii. thermal modeling. Metallurgical and Materials Transactions A **35**(6), 1869–1879 (2004). https://doi.org/10.1007/s11661-004-0095-7

[18] Sames, W.J., List, F.A., Pannala, S., Dehoff, R.R., Babu, S.S.: The metallurgy and processing science of metal additive manufacturing. International materials reviews **61**(5), 315–360 (2016). https://doi.org/10.1080/09506608.2015.111664

[19] National Academies of Sciences, Engineering, and Medicine: Methods for Enhancing Additive Manufacturing Qualification and Certification for Defense Applications: Proceedings of a Workshop—in Brief. The National Academies Press, Washington, DC (2025). https://doi.org/10.17226/28595

[20] Frazier, W.E.: An ICME informed approach to qualification for additive manufacturing. CAMBRIDGE UNIV PRESS 32 AVENUE OF THE AMERICAS, NEW YORK, NY 10013-2473 USA (2016)

[21] Das, S., Bourell, D.L., Babu, S.: Metallic materials for 3d printing. Mrs Bulletin **41**(10), 729–741 (2016). https://doi.org/10.1557/mrs.2016.217

[22] Reprinted from Materials & Design, Volume 244, Kaustubh Deshmukh, Alex

Riensche, Ben Bevans, Ryan J. Lane, Kyle Snyder, Harold (Scott) Halliday, Christopher B. Williams, Reza Mirzaeifar, Prahalada Rao, Effect of processing parameters and thermal history on microstructure evolution and functional properties in laser powder bed fusion of 316L, Pages No. 20, Copyright (2024), with permission from Elsevier

[23] Varney, T.C., Oldham, T., Noor, M.I., Rottmann, P.F.: Quantifying the microstructure and mechanical property differences between bulk and thin-wall additively manufactured inconel 718. Materialia **31**, 101867 (2023). https://doi.org/10.1016/j.mtla.2023.101867

[24] Wang, X., Chou, K.: Effects of thermal cycles on the microstructure evolution of inconel 718 during selective laser melting process. Additive Manufacturing **18**, 1–14 (2017). https://doi.org/10.1016/j.addma.2017.08.016

[25] Popovich, V., Borisov, E., Popovich, A., Sufiiarov, V.S., Masaylo, D., Alzina, L.: Functionally graded inconel 718 processed by additive manufacturing: Crystallographic texture, anisotropy of microstructure and mechanical properties. Materials & Design **114**, 441–449 (2017). https://doi.org/10.1016/j.matdes.2016.10.075

[26] Zhang, D., Niu, W., Cao, X., Liu, Z.: Effect of standard heat treatment on the microstructure and mechanical properties of selective laser melting manufactured inconel 718 superalloy. Materials Science and Engineering: A **644**, 32–40 (2015). https://doi.org/10.1016/j.msea.2015.06.021

[27] Liu, F., Lin, X., Huang, C., Song, M., Yang, G., Chen, J., Huang, W.: The effect of laser scanning path on microstructures and mechanical properties of laser solid formed nickel-base superalloy inconel 718. Journal of Alloys and Compounds **509**(13), 4505–4509 (2011). https://doi.org/10.1016/j.jallcom.2010.11.176

[28] Zhao, X., Chen, J., Lin, X., Huang, W.: Study on microstructure and mechanical properties of laser rapid forming inconel 718. Materials Science and Engineering: A **478**(1-2), 119–124 (2008). https://doi.org/10.1016/j.msea.2007.05.079

[29] Deshmukh, K., Riensche, A., Bevans, B., Lane, R.J., Snyder, K., Halliday, H.S., Williams, C.B., Mirzaeifar, R., Rao, P.: Effect of processing parameters and thermal history on microstructure evolution and functional properties in laser powder bed fusion of 316l. Materials & Design **244**, 113136 (2024). https://doi.org/10.1016/j.matdes.2024.113136

[30] Yavari, R., Williams, R., Cole, K., Hooper, P., Rao, P.: Thermal modeling in metal additive manufacturing using graph theory: experimental validation with in-situ infrared thermography data from laser powder bed fusion. In: International Manufacturing Science and Engineering Conference, vol. 84256, pp. 001–01028 (2020). American Society of Mechanical Engineers. https://doi.org/10.1115/1.4047619

[31] Yavari, R., Smoqi, Z., Riensche, A., Bevans, B., Kobir, H., Mendoza, H., Song, H., Cole, K., Rao, P.: Part-scale thermal simulation of laser powder bed fusion using graph theory: Effect of thermal history on porosity, microstructure evolution, and recoater crash. Materials & Design **204**, 109685 (2021). https://doi.org/10.1016/j.matdes.2021.109685

[32] Riensche, A., Bevans, B.D., Smoqi, Z., Yavari, R., Krishnan, A., Gilligan, J., Piercy, N., Cole, K., Rao, P.: Feedforward control of thermal history in laser powder bed fusion: Toward physics-based optimization of processing parameters. Materials & Design **224**, 111351 (2022). https://doi.org/10.1016/j.matdes.2022.111351

[33] Yavari, R., Riensche, A., Tekerek, E., Jacquemetton, L., Halliday, H., Vandever, M., Tenequer, A., Perumal, V., Kontsos, A., Smoqi, Z., *et al.*: Digitally twinned additive manufacturing: Detecting flaws in laser powder bed fusion by combining thermal simulations with in-situ meltpool sensor data. Materials & Design **211**, 110167 (2021). https://doi.org/10.1016/j.matdes.2021.110167

[34] Yavari, R., Williams, R., Riensche, A., Hooper, P.A., Cole, K.D., Jacquemetton, L., Halliday, H.S., Rao, P.K.: Thermal modeling in metal additive manufacturing using graph theory–application to laser powder bed fusion of a large volume impeller. Additive Manufacturing **41**, 101956 (2021). https://doi.org/10.1016/j.addma.2021.101956

[35] Yavari, M.R., Cole, K.D., Rao, P.: Thermal modeling in metal additive manufacturing using graph theory. Journal of Manufacturing Science and Engineering **141**(7), 071007 (2019). https://doi.org/10.1115/1.4043648

[36] Hemker, K.J., Sharpe Jr, W.N.: Microscale characterization of mechanical properties. Annu. Rev. Mater. Res. **37**(1), 93–126 (2007). https://doi.org/10.1146/annurev.matsci.36.062705.134551

[37] LaVan, D., Sharpe Jr, W.: Tensile testing of microsamples. Experimental mechanics **39**(3), 210–216 (1999). https://doi.org/10.1007/BF02323554

[38] Nimer, S.M.: Microscale mechanical experiments across temperatures: System development and material characterization. PhD thesis (2016)

[39] Duffy, M.E.: Microtensile characterization of additively manufactured alsi10mg. PhD thesis (2018)

[40] Carmo Santos, J.C.: A qualification methodology for additively manufactured parts. Master's thesis, Universidade do Porto (Portugal) (2016)

[41] Sousa, A.D.R.: Orientation and location dependency of the mechanical properties of an alsi10mg part produced using direct metal laser sintering (dmls) – a microsample approach. Master's thesis, Universidade do Porto (Portugal) (2017)

[42] Zheng, P., Chen, R., Liu, H., Chen, J., Zhang, Z., Liu, X., Shen, Y.: On the standards and practices for miniaturized tensile test–a review. Fusion Engineering and Design **161**, 112006 (2020). https://doi.org/10.1016/j.fusengdes.2020.112006

Supplementary Files

This is a list of supplementary files associated with this preprint. Click to download.

- GraphicalAbstract.png